J Mater Sci (2007) 42:6555–6565
DOI 10.1007/s10853-007-1526-9

Theoretical study of the insulating oxides and nitrides: SiO_2, GeO_2, Al_2O_3, Si_3N_4, and Ge_3N_4

Cem Sevik · Ceyhun Bulutay

Received: 5 October 2006 / Accepted: 16 January 2007 / Published online: 2 May 2007

Abstract An extensive theoretical study is performed for wide bandgap crystalline oxides and nitrides, namely, SiO_2, GeO_2, Al_2O_3, Si_3N_4, and Ge_3N_4. Their important polymorphs are considered which are for SiO_2: α-quartz, α- and β-cristobalite and stishovite, for GeO_2: α-quartz, and rutile, for Al_2O_3: α-phase, for Si_3N_4 and Ge_3N_4: α- and β-phases. This work constitutes a comprehensive account of both electronic structure and the elastic properties of these important insulating oxides and nitrides obtained with high accuracy based on density functional theory within the local density approximation. Two different norm-conserving ab initio pseudopotentials have been tested which agree in all respects with the only exception arising for the elastic properties of rutile GeO_2. The agreement with experimental values, when available, are seen to be highly satisfactory. The uniformity and the well convergence of this approach enables an unbiased assessment of important physical parameters within each material and among different insulating oxide and nitrides. The computed static electric susceptibilities are observed to display a strong correlation with their mass densities. There is a marked discrepancy between the considered oxides and nitrides with the latter having sudden increase of density of states away from the respective band edges. This is expected to give rise to excessive carrier scattering which can practically preclude bulk impact ionization process in Si_3N_4 and Ge_3N_4.

C. Sevik (✉) · C. Bulutay
Department of Physics and National Nanotechnology Research Center, Bilkent University, Ankara 06800, Turkey
e-mail: sevik@fen.bilkent.edu.tr

C. Bulutay
e-mail: bulutay@fen.bilkent.edu.tr

Introduction

Insulating oxides and nitrides are indispensable materials for diverse applications due to their superior mechanical, thermal, chemical and other outstanding high temperature properties. Furthermore, in the electronic industry these wide band gap materials are being considered for alternative gate oxides [1] and in the field of integrated optics they provide low-loss dielectric waveguides [2]. Recently the subject of wide bandgap oxides and nitrides have gained interest within the context of nanocrystals which offer silicon-based technology for light emitting devices and semiconductor memories [3]. These nanocrystals are embedded in an insulating matrix which is usually chosen to be silica [4–7]. However, other wide bandgap materials are also employed such as germania [8, 9], silicon nitride [10–12], and alumina [13–15]. As a matter of fact, the effect of different host matrices is an active research topic in this field.

Among these insulating oxides and nitrides technologically most important ones are SiO_2, Al_2O_3, Si_3N_4. The activity around GeO_2 is steadily increasing. Another closely-related material, Ge_3N_4 has attracted far less attention up to now even though it has certain interesting properties [16]. The major obstacle has been the sample growth. However, a very recent study reported an in situ Ge_3N_4 growth on Ge, demonstrating high thermal stability and large band offsets with respect to the Ge system [17]. In this comprehensive work, we present the ab initio structural and electronic properties of all these materials considering their common polymorphs; these are for SiO_2: α-quartz, α- and β-cristobalite and stishovite phases, for GeO_2: α-quartz, and rutile phases, for Si_3N_4 and Ge_3N_4: α- and β-phases and for Al_2O_3: α-phase. For amorphous and inherently imperfect matrices, these perfect crystalline

phases serve as important reference systems. Moreover, due to their distinct advantages, *epitaxial* host lattices are preferred over the amorphous ones for specific applications.

With an eye on these technological applications, we focus on several physical properties of these lattices. The elastic constants play an important role on the strain profile of the embedded core semiconductor. Using Eshelby's continuum elastic consideration [18] the radial and tangential stress fields of the nanocrystal can be determined [19]; these in turn, affect the optical properties [6]. The static and optical dielectric constants of these lattices introduce nontrivial local field effects that modify the absorption spectra of an isolated nanocrystal when embedded inside one of these matrices [20]. Based on the simple effective medium theory which has been tested by ab initio calculations [21], one can assess which host lattice and nanocrystal combination would possess the desired optical properties. Because of the dielectric mismatch between the nanocrystal core and the surrounding lattice, image charges will be produced [22]. These image charges should be taken into account in characterizing nanocrystal excitons [23]. Another promising application is the visible and near infrared electroluminescence from Si and Ge nanocrystals [3]. The electroluminescence is believed to be achieved by the recombination of the electron hole pairs injected to nanocrystals under high bias [3]. In this context the bulk state impact ionization process which can also give rise to electroluminescence is considered to be detrimental leading to dielectric breakdown. For high-field carrier transport, the crucial physical quantity was identified to be the valence and conduction band density of states (DOS) for each of the crystalline polymorph [24]. Based on these technology-driven requirements we compute the elastic constants, band structures, dielectric permittivities and electronic DOS of these aforementioned crystal polymorphs. Our ab initio framework is based on the density functional theory [25, 26], using pseudopotentials and a plane wave basis [27]. With the exception of Ge_3N_4 which was far less studied, vast amount of theoretical work is already available spread throughout the literature based on a variety of techniques [28–37]. Our first-principles study here enables a uniform comparison of important physical parameters within each material and among different insulating oxides and nitrides.

The plan of the paper is as follows: in Section ''Details of ab initio computations'' we provide details of our ab initio computations, Section ''First-principles results'' contains our first-principles results for the structural, electronic properties of the materials considered followed by our conclusions in Section ''Conclusions''.

Details of *ab initio* computations

Structural and electronic properties of the polymorphs under consideration have been calculated within the density functional theory [25, 26], using the plane wave basis pseudopotential method as implemented in the ABINIT code [27]. The results are obtained under the local density approximation (LDA) where for the exchange-correlation interactions we use the Teter Pade parameterization [38], which reproduces Perdew-Zunger [39] (which reproduces the quantum Monte Carlo electron gas data of Ceperley and Alder [40]). We tested the results under two different norm-conserving Troullier and Martins [41] type pseudopotentials, which were generated by A. Khein and D.C. Allan (KA) and Fritz Haber Institute (FHI). For both pseudopotentials, the valence configurations of the constituent atoms were chosen as N($2s^2p^3$), O($2s^2p^4$), Al($3s^2$ $3p^1$), Si($3s^2$ $3p^2$), and Ge($4s^2$ $4p^2$). The number of angular momenta of the KA (FHI) pseudopotentials and the chosen local channel were respectively, for N: 1, *p* (3, *d*), for O: 1, *p* (3, *d*), for Al: 2, *d* (3, *d*), for Si: 2, *d* (3, *d*), and for Ge: 1, *p* (3, *s*). Our calculated values for these two types of pseudopotentials were very similar, the only exceptional case being the elastic constants for rutile GeO_2. Dielectric permitivity and the fourth-order tensor of elastic constants of each crystal are determined by starting from relaxed unit cell under the application of finite deformations within density functional perturbation theory [42] as implemented in ABINIT and ANADDB extension of it. Another technical detail is related with the element and angular momentum-resolved partial density of states (PDOS). To get a representative PDOS behavior we need to specify the spherical regions situated around each relevant atomic site. The radii of these spheres are chosen to partition the bond length in proportion to the covalent radii of the constituent atoms. This resulted in the following radii: for the α-quartz SiO_2, r_{Si} = 0.97 Å, r_O = 0.65 Å, for the rutile GeO_2, r_{Ge} = 1.16 Å, r_O = 0.69 Å, for the α-Al_2O_3, r_{Al} = 1.32 Å, r_O = 0.56 Å, and for the β-Si_3N_4, r_{Si} = 1.03 Å, r_N = 0.70 Å. It should be pointed that even though such an approach presents a good relative weight of the elements and angular momentum channels, it inevitably underestimates the total DOS, especially for the conduction bands. Other details of the computations are deferred to the discussion of each crystal polymorph.

First-principles results

First, we address the general organization and the underlying trends of our results. The lattice constants and other structural informations of all crystals are listed in Table 1. Table 2 contains the bond lengths and bond angles of the

Table 1 Structural information on crystals

Crystal	Crystal structure	Lattice constants (Å)	Space group	Molecules per prim. cell	Density (gr/cm^3)
α-quartz SiO_2	Hexagonal	a = 4.883[a] 4.854[b] 4.913[c]	$P3_221$	3	2.698
		c = 5.371[a] 5.341[b] 5.405[c]			
α-cris. SiO_2	Tetragonal	a = 4.950[a] 4.939[b] 4.973[c]	$P4_12_12$	4	2.372
		c = 6.909[a] 6.894[b] 6.926[c]			
β-cris. SiO_2	Cubic	a = 7.403[a] 7.330[b] 7.160[c]	$Fd3m$	2	1.966
Stishovite SiO_2	Tetragonal	a = 4.175[a] 4.145[b] 4.179[d]	$P4_2/mnm$	2	4.298
		c = 2.662[a] 2.643[b] 2.665[d]			
α-quartz GeO_2	Hexagonal	a = 4.870[a] 4.861[b] 4.984[f]	$P3_221$	3	4.612
		c = 5.534[a] 5.520[b] 5.660[f]			
Rutile GeO_2	Tetragonal	a = 4.283[a] 4.314[b] 4.4066[g]	$P4_2/mnm$	2	6.655
	Tetragonal	c = 2.782[a] 2.804[b] 2.8619[g]			
α-Al_2O_3	Rombohedral	a = 4.758[a] 4.762[e]	$R\bar{3}c$	2	3.992
		c = 12.98[a] 12.896[e]			
α-Si_3N_4	Hexagonal	a = 7.732[a] 7.766[h]	C_{3v}^4	4	3.211
		c = 5.603[a] 5.615[h]			
β-Si_3N_4	Hexagonal	a = 7.580[a] 7.585[i]	C_{6h}^2	2	3.229
		c = 2.899[a] 2.895[i]			
α-Ge_3N_4	Hexagonal	a = 7.985[a]	C_{3v}^4	4	5.691
		c = 5.786[a]			
β-Ge_3N_4	Hexagonal	a = 7.826[a]	C_{6h}^2	2	5.727
		c = 2.993[a]			

[a] This work KA
[b] This work FHI
[c] Ref. [43]
[d] Ref. [44]
[e] Ref. [31]
[f] Ref. [45]
[g] Refs. [46, 47]
[h] Ref. [32]
[i] Ref. [37]

optimized oxide polymorphs. These results can be used to identify the representation of each polymorph within the amorphous oxides [52]. The elastic constants and dielectric permittivity tensor of each crystal are tabulated in Table 3 and Table 4, respectively. Very close agreement with the existing experimental data and previous calculations can be observed which gives us confidence about the accuracy and convergence of our work. Employing KA pseudopotentials, the band structure for the crystals are displayed along the high-symmetry lines in Figs. 1–4 together with their corresponding total DOS. Such an information is particlulary useful in the context of high-field carrier transport. These results are in good agreement with the previous computations [29, 32, 35, 36]. For all of the considered polymorphs the conduction band minima occur at the Γ point whereas the valence band maxima shift away from this point for some of the phases making them indirect band gap matrices (see Table 5). However, the direct band gap values are only marginally above the indirect band gap values. These LDA band gaps are underestimated which is a renown artifact of LDA for semiconductors and insulators [59]. In this work we do not attempt any correction procedure to adjust the LDA band gap values.

We present in Figs. 5–7 the element- and angular momentum-resolved PDOS. A common trend that can be observed in these various lattices is that their valence band maxima are dominated by the p states belonging to O atoms; in the case of Si_3N_4 and Ge_3N_4 they are the N atoms. For the conduction band edges, both constituent elements have comparable contribution. This parallels the observation in amorphous SiO_2 where due to large electronegativity difference between Si and O, the bonding orbitals have a large weight on O atoms whereas the lowest conduction band states with antibonding

Table 2 Bond lengths and bond angles (in degrees) of SiO_2 and GeO_2 polymorphs where x represents a Si or a Ge atom

Crystal		x–O (Å)	x–O (Å)	O–x–O	O–x–O	O–x–O	O–x–O	x–O–x	x–O–x
α-quartz SiO_2	This work	1.613	1.618	110.75	109.32	109.07	108.47	140.55	
	Exp.[a]	1.605	1.614	110.50	109.20	109.00	108.80	143.7	
α-quartz GeO_2	This work	1.693	1.699	113.03	110.62	107.94	106.16	130.56	
α-cris. SiO_2	This Work	1.597	1.596	111.59	110.08	109.03	108.02	146.02	
	Exp.[b]	1.603	1.603	111.40	110.00	109.00	108.20	146.5	
β-cris. SiO_2	This work	1.603		109.47				180	
	Exp.[c]	1.611		107.80				180.00	
Stishovite SiO_2	This work	1.804	1.758	98.47	81.53			130.76	98.47
	Exp.[d]	1.760	1.810					130.60	
Rutile GeO_2	This Work	1.848	1.824	99.34	80.66			99.34	130.33

[a] Ref. [48]

[b] Ref. [49]

[c] Ref. [50]

[d] Ref. [51]

character have a significant contribution from the Si atoms [60].

From another perspective, the band structures and the associated DOS reveal that there is a marked discrepancy between the valence and conduction band edges where for the former there occurs a sharp increase of DOS just below the band edge. As the probabilities of most scattering processes are directly proportional to DOS [61], in the case of high-field carrier transport the electrons should encounter far less scatterings and hence gain much higher energy from the field compared to holes. In this respect Si_3N_4 and Ge_3N_4 are further different from the others where for both conduction and valence bands the DOS dramatically increases (cf. Fig. 4) so that the carriers should suffer from excessive scatterings which practically precludes the bulk impact ionization for this material.

Another common trend can be investigated between the density of each polymorph and the corresponding static permittivity, ε_s. Such a correlation was put forward by Xu and Ching among the SiO_2 polymorphs [29]. We extend this comparison to all structures considered in this work and rather use $\chi_e = \varepsilon_{s-1}$ which corresponds to electric susceptibility. It can be observed from Fig. 8 that the trend established by SiO_2 polymorphs is also followed by β-Si_3N_4 and α-Al_2O_3. On the other hand, Ge-containing structures while possessing a similar trend among themselves, display a significant shift due to much higher mass of the this atom. This dependence on the atomic mass needs to be removed by finding a more suitable physical quantity. We should mention that such a correlation does not exist between the volume per primitive cell of each phase and the static permittivity. After these general comments, now we concentrate on the results of each lattice individually.

SiO_2

The α-quartz SiO_2 is one of the most studied polymorphs as it is the stable phase at the ambient pressure and temperature [30, 34], furthermore its short-range order is essentially the same as the amorphous SiO_2 [60]. α-quartz SiO_2 has a hexagonal unit cell containing three SiO_2 molecules. A plane-wave basis set with an energy cutoff of 60 Ha was used to expand the electronic wave functions at the special k-point mesh generated by $10 \times 10 \times 8$ Monkhorst-Pack scheme [62]. The band structure of α-quartz SiO_2 has been calculated by many authors (see, for instance [28, 29]). Our calculated band structure and total DOS shown in Fig. 1a are in agreement with the published studies [29]. The indirect LDA band gap for this crystal is 5.785 eV from the valence band maximum at K to the conduction band minimum at Γ. The direct LDA band gap at Γ is slightly larger than the indirect LDA band gap as seen in Table 5. Calculated values of the elastic constants and bulk modulus listed in Table 3 are in good agreement with the experiments. Apart from C_{12}, the elastic constants are within 10% of the experimental values. The discrepancy in C_{12} can be explained by the fact that C_{12} is very soft and this type of deviation also exists among experiments which is also the case for C_{14}.

α-cristobalite SiO_2 has a tetragonal unit cell containing four SiO_2 molecules. In the course of calculations an absolute energy convergence of 10^{-4} Ha was obtained by setting a high plane wave energy cutoff as 60 Ha and

Table 3 Elastic constants and bulk modulus for each crystal

Crystal	(GPa)	C_{11}	C_{12}	C_{13}	C_{14}	C_{33}	C_{44}	C_{66}	B
α-quartz SiO_2	KA	76.2	11.9	11.2	–17.0	101.7	54.0	32.1	35
	FHI	79.5	9.73	9.54	–18.9	101.7	55.5	34.9	35
	Exp.[a]	87.0	7.00	13.0	–18.0	107.0	57.0	40.0	38
	Exp.[b]	87.0	7.00	19.0	–18.0	106.0	58.0		40
α-Cris. SiO_2	KA	49.30	5.26	–11.41		44.78	74.15	26.85	12
β-Cris. SiO_2	KA	194.0	135.0				82.67		155
	FHI	196.1	134.2				85.40		155
Stishovite SiO_2	KA	447.7	211.0	203.0		776.0	252.0	302.0	306
	FHI	448.8	211.1	191.0		752.0	256.5	323.0	302
	Exp.[c]	453.0	211.0	203.0		776.0	252.0	302.0	308
α-quartz GeO_2	KA	66.7	24.3	23.1	–3.00	118.7	41.3	21.2	41
	FHI	63.8	25.7	26.2	–0.81	120.2	35.3	19.1	42
	Exp.[d]	66.4	21.3	32.0	–2.20	118.0	36.8	22.5	42
	Exp.[b]	64.0	22.0	32.0	–2.00	118.0	37.0	21.0	42
Rutile GeO_2	KA	405.9	235.3	189.2		672.4	206.0	314.4	292
	FHI	349.2	197.2	185.1		617.5	171.8	274.8	258
	Exp.[e]	337.2	188.2	187.4		599.4	161.5	258.4	251
α-Al_2O_3	KA	493.0	164.1	130.1		485.8	155.5	164.4	258
	Exp.[f]	497.0	164.0	111.0		498.0	147.0		251
β-Si_3N_4	KA	421.8	197.8	116.6		550.7	100.2	112.0	250
	Exp.[g]	433.0	195.0	127.0		574.0	108.0	119.0	259
	Exp.[h]	439.2	181.8	149.9		557.0	114.4	135.9	265
β-Ge_3N_4	KA	364.3	184.9	111.7		486.3	80.4	89.7	225

[a] Ref. 53
[b] Ref. 54
[c] Ref. 55
[d] Ref. 45
[e] Ref. 47
[f] Ref. 56
[g] Ref. 57
[h] Ref. 58

Table 4 Dielectric permittivity tensor

Crystal	$\epsilon^0_{xx} = \epsilon^0_{yy}$	ϵ^0_{zz}	$\epsilon^\infty_{xx} = \epsilon^\infty_{yy}$	ϵ^∞_{zz}
α-quartz SiO_2	4.643	4.847	2.514	2.545
α-cris. SiO_2	4.140	3.938	2.274	2.264
β-cris. SiO_2	3.770	3.770	2.078	2.078
Stishovite SiO_2	10.877	8.645	3.341	3.510
α-quartz GeO_2	5.424	5.608	2.864	2.947
Rutile GeO_2	10.876	8.747	3.679	3.945
α-Al_2O_3	10.372	10.372	3.188	3.188
β-Si_3N_4	8.053	8.053	4.211	4.294
β-Ge_3N_4	8.702	8.643	4.558	4.667

$10 \times 10 \times 8$ k-point sampling. Figure 1b shows the band structure of α-cristobalite SiO_2 with the 5.525 eV direct band gap at Γ. The bulk modulus of 12 GPa is the smallest among all the host lattice polymorphs considered in this work.

Regarding β-cristobalite, its actual structure is somewhat controversial, as a number of different symmetries have been proposed corresponding to space groups $Fd3m$, $I\bar{4}2d$, and $P2_13$ [34]. Recently, incorporating the quasiparticle corrections the tetragonal $I\bar{4}2d$ phase was identified to be energetically most stable [63]. However, we work with the structure having the space group of $Fd3m$ that was originally proposed by Wyckoff [64] and which is widely studied primarily due to its simplicity [28, 30]. This phase has a cubic conventional cell with two molecules. We used 60 Ha plane wave energy cutoff and $10 \times 10 \times 10$ k-point sampling. Figure 1c shows the band structure of β-cristobalite SiO_2 with the 5.317 eV direct band gap at Γ. Unlike their band structures, total DOS of α- and and β-cristobalite SiO_2 are very similar (cf. Fig. 1c).

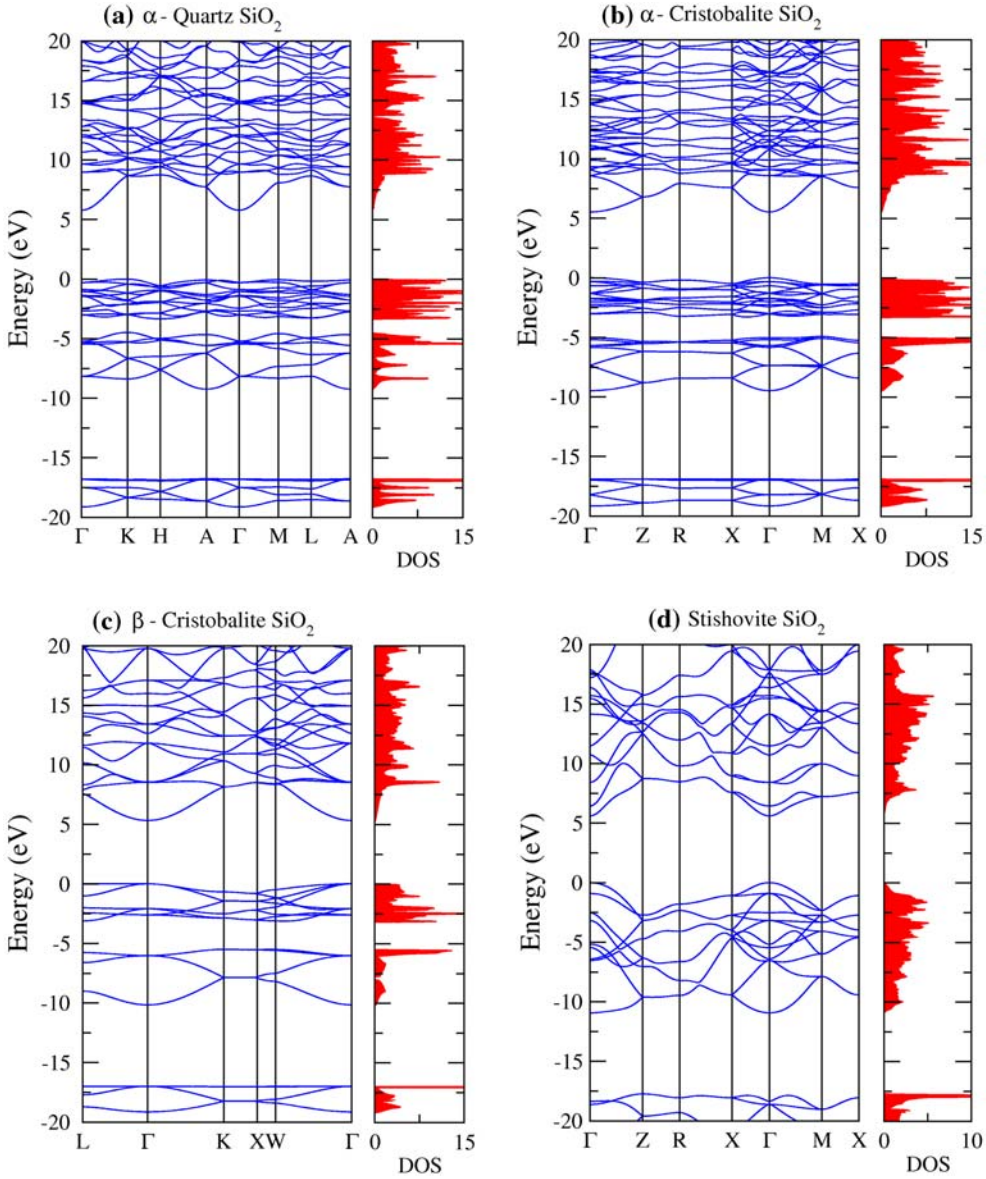

Fig. 1 LDA band structure and total DOS (electrons/eV cell) of (**a**) α-cristobalite SiO_2, (**b**) α-quartz SiO_2, (**c**) β-cristobalite SiO_2, and (**d**) stishovite SiO_2

This similarity can be explained by the fact that their local structure are very close. On the other hand there is a considerable difference between the DOS spectra of the α-quartz SiO_2 and the β-cristobalite SiO_2. In Table 3, we present elastic constants of the β-cristobalite SiO_2 calculated by two types of pseudopotentials, FHI and KA. There is no considerable difference between them. Dielectric constants of β-cristobalite SiO_2 are the smallest among the five polymorphs of SiO_2 studied here (see Table 4).

Stishovite is a dense polymorph of SiO_2 with octahedrally coordinated silicon, unlike the previous phases [34]. It has a tetragonal cell with two molecules. Calculations were done by using 60 Ha plane wave energy cutoff and $8 \times 8 \times 10$ k-point sampling. The band structure of stishovite with a wide single valence band is markedly different from that of the previous three crystalline phases of SiO_2 having two narrow upper valence bands. The cause of this increased valence bandwidth is the lack of separation between bonding and nonbonding states [36]. Hence, the total DOS for stishovite shows no gap at the middle of the valence band (see Fig. 1d). Our calculations yield a direct LDA band gap of 5.606 eV at Γ. As seen in Table 3, the differences between our computed elastic constants and the experimental values are less than 3%; this is an excellent agreement for LDA. Its bulk modulus is the largest among all the host lattice polymorphs considered in this work. Moreover, dielectric constants of stishovite is the largest of the five polymorphs of SiO_2 considered in this work (see Table 4).

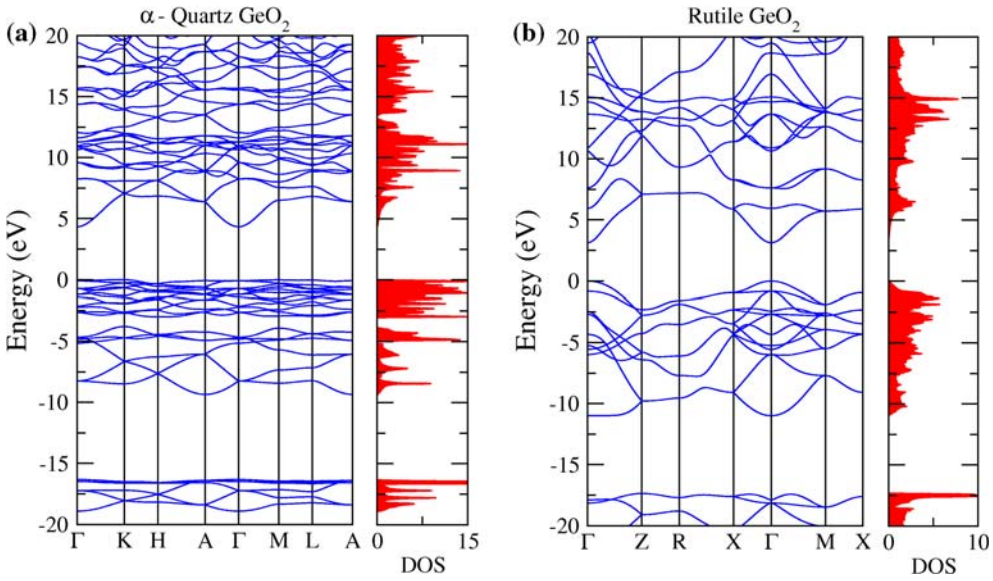

Fig. 2 LDA band structure and total DOS of (**a**) α-quartz GeO_2, (**b**) rutile GeO_2

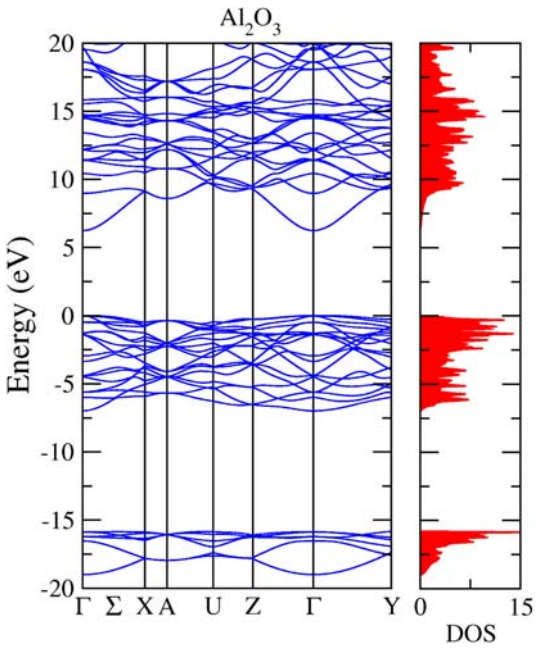

Fig. 3 LDA band structure of and total DOS of α-Al_2O_3

GeO_2

For α-quartz GeO_2 we used the same energy cutoff and *k*-point sampling as with α-quartz SiO_2 which yields excellent convergence. The band structure of the α-quartz GeO_2 is displayed in Fig. 2a. The similarity of the band structures of the α-quartz GeO_2 and the α-quartz SiO_2 is not surprising as they are isostructural. Similarly their total DOS resemble each other (cf. Fig. 2a). The indirect LDA band gap for this phase is 4.335 eV from the valence band maximum at *K* to the conduction band minimum at Γ. The direct band gap at Γ is slightly different from indirect band gap as seen in Table 5. This gap is smaller than that of the α-quartz SiO_2. The perfect agreement between calculated elastic constants of the α-quartz GeO_2 and experimental values [45, 54] can be observed in Table 3.

The rutile structure of GeO_2, also known as argutite [65] is isostructural with the stishovite phase of SiO_2. The same energy cutoff and *k*-point sampling values as for stishovite yield excellent convergence. The direct LDA band gap at Γ for rutile-GeO_2 is less than that of stishovite with a value of 3.126 eV. The two upper valence bands are merged in the total DOS (see Fig. 2b) as in the case of stishovite. The increased valence bandwidth in the band structure can be explained by the same reason as in the case of stishovite. The results of the elastic constants calculated with KA type pseudopotential shown in Table 3 deviate substantially from the experiment whereas the agreement with the FHI pseudopotentials is highly satisfactory. The similarity of the dielectric constants of rutile GeO_2 and stishovite can be observed in Table 4.

Al_2O_3

Al_2O_3 is regarded as a technologically important oxide due to its high dielectric constant and being reasonably a good glass former after SiO_2 [1]. The α-Al_2O_3 (sapphire) has the rhombohedral cell with two molecules. Computations about Al_2O_3 were done by using 60 Ha plane wave energy cutoff and a total of 60 *k*-points within the Brillouin zone. Figure 3 shows the computed band structure and total DOS of the α-Al_2O_3. These are in excellent agreement with the previous calculation [31, 33]. For Al_2O_3, minimum of the conduction band is at Γ and maximum of the valence band is at a point along Γ–*X* close to the Γ point. The corre-

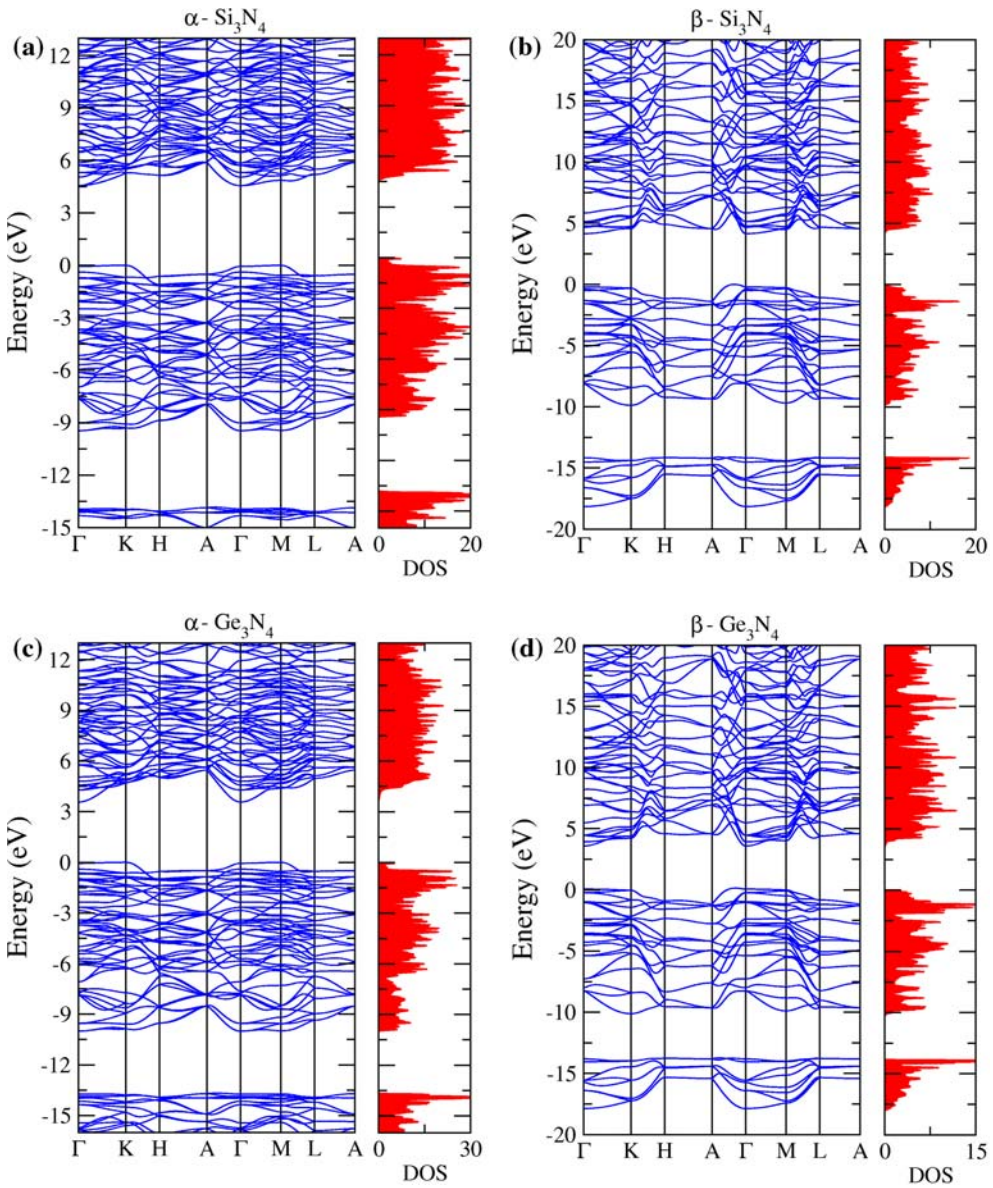

Fig. 4 LDA band structure and total DOS of (**a**) α-Si_3N_4; (**b**) β-Si_3N_4; (**c**) α-Ge_3N_4 and (**d**) β-Ge_3N_4

Table 5 Indirect (E_g) and direct ($E_g(\Gamma)$) LDA Band Gaps for each crystal

Crystal	VB Max.	CB Min.	E_g (eV)	$E_g(\Gamma)$ (eV)
α-quartz SiO_2	K	Γ	5.785	6.073
α-cris. SiO_2	Γ	Γ	5.525	5.525
β-cris. SiO_2	Γ	Γ	5.317	5.317
Stishovite SiO_2	Γ	Γ	5.606	5.606
α-quartz GeO_2	K	Γ	4.335	4.434
Rutile GeO_2	Γ	Γ	3.126	3.126
α-Al_2O_3	Γ	Γ	6.242	6.242
α-Si_3N_4	M	Γ	4.559	4.621
β-Si_3N_4	A-Γ	Γ	4.146	4.365
α-Ge_3N_4	M	Γ	3.575	3.632
β-Ge_3N_4	A-Γ	Γ	3.447	3.530

sponding LDA band gap is 6.242 eV. Because of the very small difference between the direct and indirect band gaps, Al_2O_3 is considered as a direct band gap insulator. Measured band gap of this crystal is 8.7 eV. However the precise value of the gap of Al_2O_3 is still elusive because of the existence of an excitonic peak near the absorbtions edge [66]. As seen in Table 3, computed values of the elastic constant and bulk modulus of Al_2O_3 are in excellent agreement with the experiments. As a further remark, the α-Al_2O_3 unit cell can be described as hexagonal or rhombohedral depending on the crystallographical definition of the space group $R\bar{3}C$. During our first-principles calculations it has been defined as rhombohedral in which case C_{14} vanishes. Although the sign of C_{14} is experimentally determined to be negative for the hexagonal-Al_2O_3,

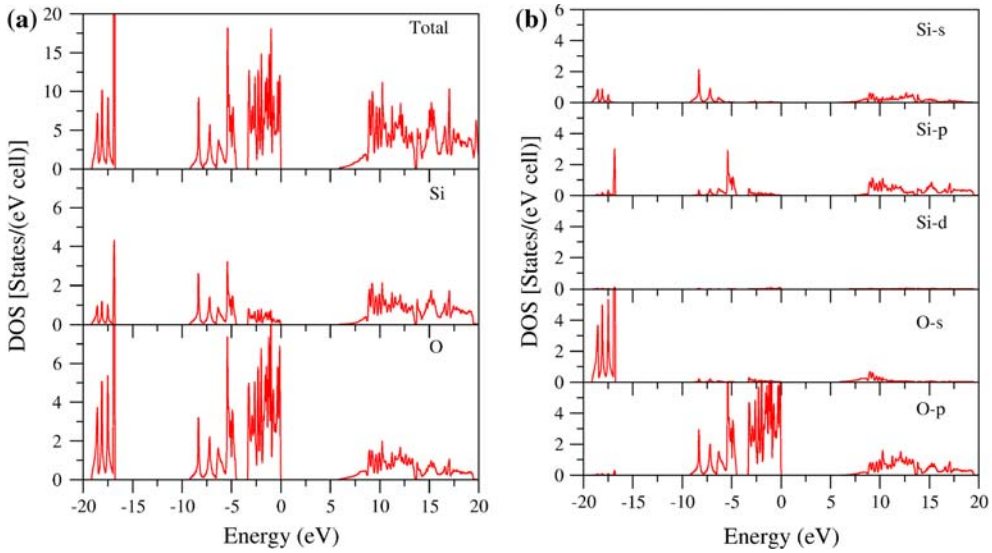

Fig. 5 DOS of α-quartz SiO_2 (**a**) Element-resolved; total, PDOS of Si, PDOS of O; (**b**) Angular momentum-resolved; Si *s* electrons, Si *p* electrons, Si *d* electrons (not visible at the same scale), O *s* electrons, O *p* electrons.

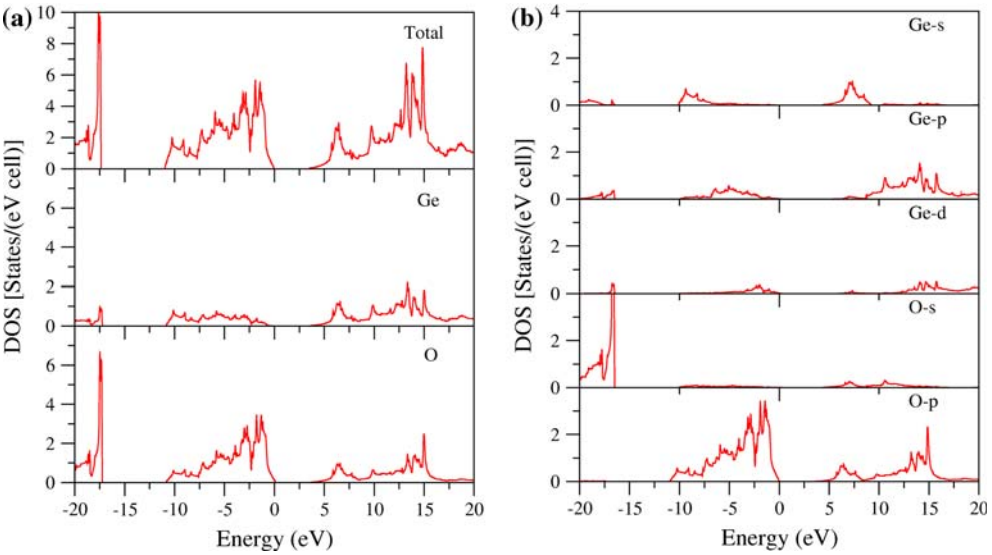

Fig. 6 DOS of rutile GeO_2 (**a**) Element-resolved; total PDOS of Ge, PDOS of O; (**b**) Angular momentum-resolved; Ge *s* electrons, Ge *p* electrons, Ge *d* electrons, O *s* electrons, O *p* electrons

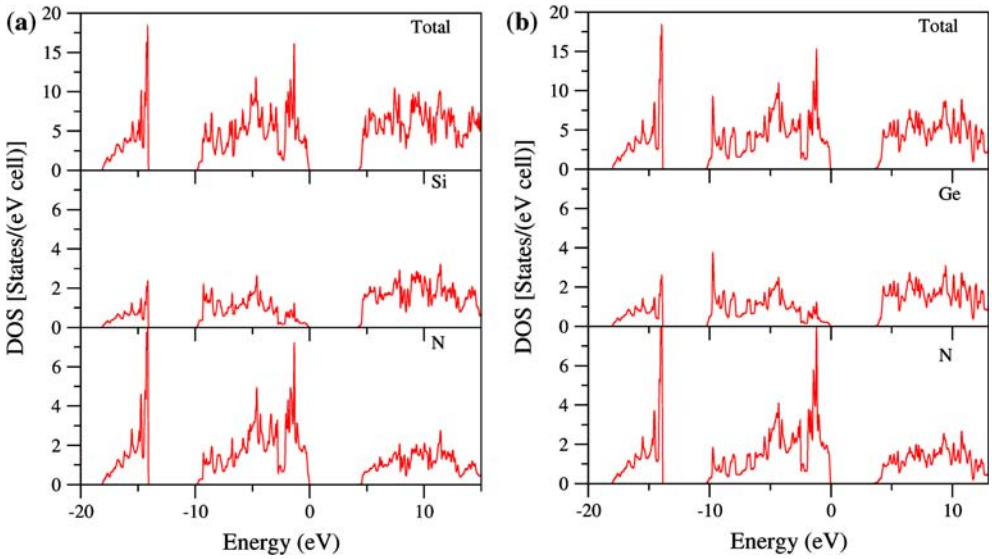

Fig. 7 Element-resolved DOS of (**a**) β-Si_3N_4; total, PDOS of Si, PDOS of N, (**b**) β-Ge_3N_4; total, PDOS of Ge, PDOS of N

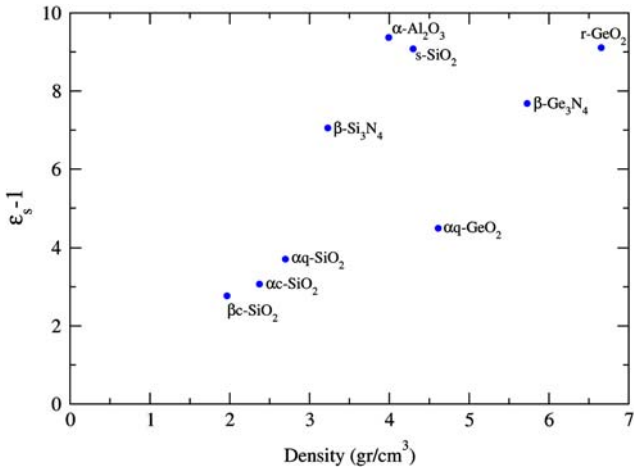

Fig. 8 Density versus direction-averaged static electric susceptibility

previous calculations reported a positive value [67]. To check this disagreement we have calculated the elastic constant of the hexagonal-Al_2O_3 and found it to be around –3.0.

Si_3N_4 and Ge_3N_4

The research on silicon nitride has largely been driven by its use in microelectronics technology to utilize it as an effective insulating material and also as diffusion mask for impurities. Recently it started to attract attention both as a host embedding material for nanocrystals [10–12] and also for optical waveguide applications [2]. The α- and β-Si_3N_4 have hexagonal conventional cells with four and two molecules, respectively. We used 60 Ha plane wave energy cutoff and $6 \times 6 \times 8$ k-point sampling. The computed band structures of these two phases shown in Fig. 4a and b are identical to those reported by Xu and Ching [32]. The top of the valence band for β-Si_3N_4 is along the Γ-A direction, and for α-Si_3N_4 it is at the M point. The bottom of the conduction band for two phases are at the Γ point. The direct and indirect LDA band gaps of these two phases are respectively, 4.559, 4.621 eV for α-Si_3N_4 and 4.146, 4.365 eV for the β-Si_3N_4. The general band structure of two phases are very similar, except that the α-Si_3N_4 has twice as many bands because the unit cell is twice as large. The total DOS of these two phases shown in Fig. 4a and b are only marginally different. Calculated values of the elastic constants and bulk modulus of β-Si_3N_4 listed in Table 3 are in excellent agreement with the quoted experiments. Those for the α-Si_3N_4 which is thermodynamically less stable with respect to β-phase [68] were left out due to excessive memory requirements for the desired accuracy.

Ge_3N_4 is the least studied material among the oxides and nitrides considered in this work. Recently its high-pressure γ-phase has attracted some theoretical interest [69]. However, the available Ge_3N_4 samples contain a mixture of α and β-phases as in the case of Si_3N_4 and these are the polymorphs that we discuss in this work. The band structures of both of these phases of Ge_3N_4 (cf. Fig. 4) are very similar to those of Si_3N_4. Regarding the elastic constants of β-Ge_3N_4, our theoretical results listed in Table 3 await experimental verification. In terms of density, the β phases of Si_3N_4 and Ge_3N_4 fill the gap between the α-quartz and stishovite/rutile phases of their oxides. As can be observed from Fig. 8 their electric susceptibility versus density behavior strengthens the correlation established by the remaining polymorphs. Finally it should be pointed that β-Ge_3N_4 has the largest high-frequency dielectric constant (ε_∞) among all the materials considered in this work.

Conclusions

A comprehensive first-principles study is presented which is unique in analyzing common polymorphs of the technologically-important insulating oxides and nitrides: SiO_2, GeO_2, Al_2O_3, Si_3N_4, and Ge_3N_4. The structural parameters, elastic constants, static and optical dielectric constants are obtained in close agreement with the available results. The computed dielectric constants are observed to display a strong correlation with their mass densities. For all of the considered polymorphs the conduction band minima occur at the Γ point whereas the valence band maxima shift away from this point for some of the phases making them indirect band gap matrices. However, the direct band gap values are only marginally above the indirect band gap values. The investigation of band structure and DOS data reveal that the holes in all polymorphs considered and the electrons for the case of Si_3N_4 and Ge_3N_4 should suffer excessive scatterings under high applied field which will preclude bulk impact ionization for these carrier types and polymorphs. This can be especially important for applications vulnerable to dielectric breakdown.

Acknowledgements This work has been supported by the European FP6 Project SEMINANO with the contract number NMP4 CT2004 505285. We would like to thank R. Eryiğit, T. Gürel, O. Gülseren, D. Çakır and T. Yıldırım for their useful advices and to Dr. Can Uğur Ayfer for the access to Bilkent University Computer Center facilities.

References

1. Robertson J (2006) Rep Prog Phys 69:327
2. Ay F, Aydinli A (2004) Opt Matl 26:33
3. Ossicini S, Pavesi L, Priolo F (2003) Light emitting silicon for microphotonics. Springer, Berlin
4. Hayashi S, Nagareda T, Kanzawa Y, Yamamoto K (1993) Jpn J Appl Phys 32:3840

5. Iacona F, Franzó G, Spinella C (2000) J Appl Phys 87:1295
6. Wang YQ, Kong GL, Chen WD, Diao HW, Chen CY, Zhang SB, Liao XB (2002) Appl Phys Lett 81:4174
7. Serincan U, Aygun G, Turan R (2005) J Lumin 113:229
8. Volodin VA, Gorokhov EB, Efremov MD, Marin DV, Orekhov DA (2003) JETP Lett 77:411
9. Gorokhov EB, Volodin VA, Marin DV, Orekhov DA, Cherkov AG, Gutakovskii AK, Shvets VA, Borisov AG, Efremov MD (2005) Semiconductors 39:1168
10. Volodin VA, Efremov MD, Gritsenko VA (1997) Solid State Phenom 57–58:501
11. Steimle RF, Sadd M, Muralidhar R, Rao R, Hradsky B, Straub S, White BE (2003) IEEE Trans Nanotechnol 2:335
12. Choi S, Yang H, Chang M, Baek S, Hwang H, Jeon S, Kim J, Kim C (2005) Appl Phys Lett 86:251901
13. Tognini P, Andreani LC, Geddo M, Stella A, Cheyssac P, Kofman R, Migliori A (1996) Phys Rev B 53:6992
14. Wan Q, Lin CL, Liu WL, Wang TH (2003) Appl Phys Lett 82:4708; Wan Q, Lin CL, Zhang NL, Liu WL, Yang G, Wang TH (2003) Appl Phys Lett 82:3162
15. Tetelbaum DI, Mikhaylov AN, Gorshkov ON, Kasatkin AP, Belov AI, Gaponova DM, Morozov SV (2005) Vacuum 78:519
16. Chambouleyron I, Zanatta AR (1998) J Appl Phys 84:1
17. Wang SJ, Chai JW, Pan JS, Huan ACH (2006) Appl Phys Lett 89:022105
18. Eshelby JD (1957) Proc R Soc London A 241:376
19. Balasubramanian S, Ceder G, Kolenbrander KD (1996) J Appl Phys 79:4132
20. Weissker H-Ch, Furthmüller J, Bechstedt F (2002) Phys Rev B 65:155328
21. Weissker H-Ch, Furthmüller J, Bechstedt F (2003) Phys Rev B 67:165322
22. Efremov NA, Pokutnii SI (1985) Soviet Phys Solid St 27:27; ibid., 32, (1990) 955.
23. Brus LE (1986) IEEE Trans J Quant Electron 22:1909
24. Fischetti MV, Higman JM (1991) In: Hess Kluwer K (ed) Monte Carlo device simulation: full band and beyond. Dordrecht
25. Hohenberg P, Kohn W (1964) Phys Rev 136:B864
26. Kohn W, Sham LJ (1965) Phys Rev 140:A1133
27. Gonze X, Beuken JM, Caracas R, Detraux F, Fuchs M, Rignanese GM, Sindic L, Verstraete M, Zerah G, Jollet F, Torrent M, Roy A, Mikami M, Ghosez P, Raty JY, Allan DC (2002) Comput Mater Sci 25:478
28. Li YP, Ching WY (1985) Phys Rev B 31:2172
29. Xu Y, Ching WY (1991) Phys Rev B 44:11048
30. Tetelbaum DI, Mikhaylov AN, Gorshkov ON, Kasatkin AP, Belov AI, Gaponova DM, Morozov SV (2005) Vacuum 78:519; Liu F, Garofalini S, King-Smith D, Vanderbilt D (1994) Phys Rev B 49:12528
31. Ching WY, Xu YN (1994) J Am Ceram Soc 77:404
32. Xu YN, Ching WY (1995) Phys Rev B 51:17379
33. Mo SD, Ching WY (1998) Phys Rev B 57:15219
34. Demuth T, Jeanvoine Y, Hafner J, Ángyán JG (1999) J Phys: Condens Matter 11:3833
35. Holm B, Ahuja R, Yourdshahyan Y, Johansson B, Lundqvist BI (1999) Phys Rev B 59:12777
36. Christie DM, Chelikowsky JR (2000) Phys Rev B 62:14703
37. Idrobo JC, Iddir H, Öğüt S, Ziegler A, Browning ND, Ritchie RO (2005) Phys Rev B 72:241301
38. Goedecker S, Teter M, Huetter J (1996) Phys Rev B 54:1703
39. Perdew JP, Zunger A (1981) Phys Rev B 23:5048
40. Ceperley DM, Alder BJ (1980) Phys Rev Lett 45:566
41. Troullier N, Martins JL (1990) Solid State Commun 74:613; Phys Rev B 43, 1993 (1991); Phys Rev B 43 (1991) 8861
42. Gonze X, Lee C (1997) Phys Rev B 55:10355
43. Wyckoff RWG (1965) Crystal structure. Interscience, New York
44. Baur WH, Khan AA (1971) Acta Crystallogr Sec B-27:2133
45. Balitskǐı DB, Sil'vestrova OYu, Balitskǐı, VS, Pisarevski YuV, Pushcharovski; DYu, Philippot E (2000) Crystallogr Rep 45:145
46. Bolzan AA, Fong B, Kennedy JB, Howard ChJ (1997) Acta Crystallogr Sect B: Struct Sci B 53:373
47. Wang H, Simmons G (1973) J Geophys Res 78:1262
48. Levien L, Prewitt CT (1981) Am Mineral 66:324
49. Downs RT, Palmer DC (1994) Am Mineral 79:9
50. Wright AF, Leadbetter AJ (1975) Phil Mag 31:1391
51. Sugiyama M, Endo S, Koto K (1987) Mineral J Japan 13:455
52. Van Ginhoven RM, Jónsson H, Corrales LR (2005) Phys Rev B 71:024208
53. Mcskimin J, Andreatch P, Thurston RN (1987) J Appl Phys 36:1624
54. Grimsditch M, Polian A, Brazhkin V, Balitskǐı D (1998) J Appl Phys 83:3018
55. Weidner DJ, Bass JD, Ringwood AE, Sinclair W (1982) Geophys Res Lett 87:4740
56. Watchman J Jr, Teft EE, Lam DG Jr, Stinchfield RP (1960) J Res Natl Bur Stand 64:213
57. Vogelgesang R, Grimsditch M, Wallace JS (2000) Appl Phys Lett 76:982
58. Wendel JA, Goddard WA III (1992) J Chem Phys 97:5048
59. Theory of the Inhomogenious Electron Gas (1983) Lundqvist S, March NH (eds) Plenum, New York, and references therein
60. Sarnthein J, Pasquarello A, Car R (1995) Phys Rev Lett 74:4682
61. Ridley BK (1999) Quantum processes in semiconductors. Oxford University Press, Oxford
62. Monkhorst HJ, Pack JD (1976) Phys Rev B 13:5188
63. Ramos LE, Furthmüller J, Bechstedt F (2004) Phys Rev B 69:085102
64. Wyckoff WL (1925) Am J Sci 9:448; 26 (2004) 33
65. Roberts WL, et al (1990) Encyclopedia of Minerals, 2d edn. Van Nostrand Reinhold, New York
66. French RH (1990) J Am Ceram Soc 73:447
67. Page YL, Saxe P (2002) Phy Rev B 65:104104
68. Weiss J (1981) Annu Rev Mater Sci 11:381
69. Dong J, Sankey OF, Deb SK, Wolf G, McMillan PF (2000) Phys Rev B 61:11979